Published in final edited form as:
ACS Appl Mater Interfaces. 2019 May 15; 11(19): 17256–17269. doi:10.1021/acsami.9b04283.

Mechanically Strong Silica-Silk Fibroin Bioaerogel: A Hybrid Scaffold with Ordered Honeycomb Micromorphology and Multiscale Porosity for Bone Regeneration

Hajar Maleki[1,*], **Mohammad-Ali Shahbazi**[2,3,*], **Susan Montes**[4], **Seyed Hojjat Hosseini**[5], **Mohammad Reza Eskandari**[6], **Stefan Zaunschirm**[7], **Thomas Verwanger**[8], **Sanjay Mathur**[1], **Barbara Milow**[1,9], **Barbara Krammer**[7], **Nicola Hüsing**[4]

[1]Insititue of Inorganic Chemistry, Department of Chemistry, University of Cologne, of Inorganic Chemistry, Greinstraße 6, 50939, Cologne, Germany

[2]Department of Micro- and Nanotechnology, Technical University of Denmark, DK-2800 Kgs, Lyngby, Denmark

[3]Department of Pharmaceutical Nanotechnology, School of Pharmacy, Zanjan University of Medical Sciences, 45139-56184 Zanjan, Iran

[4]Department of Chemistry and Physics of Materials, Paris-Lodron University of Salzburg, Jakob-Haringerstr. 2A-5020, Salzburg, Austria

[5]Department of Pharmacology, School of Medicine, Zanjan University of Medical Sciences, Zanjan, 45139-56184, Iran

[6]Department of Pharmacology and Toxicology, School of Pharmacy, Zanjan University of Medical Sciences, 4513956111, Zanjan, Iran

[7]University of Applied Sciences Upper Austria, Franz-Fritsch-Straße 11, 4600, Wels, Austria

[8]Department of Biosciences, Paris-Lodron University Salzburg, Hellbrunnerstr. 34, 5020, Salzburg, Austria

[9]Department of Aerogels and Aerogel Composites, Institute of Materials Research, German Aerospace Center (DLR), Linder Höhe 51147, Cologne, Germany

Abstract

Due to the synergic feature of individual components in hybrid (nano)biomaterials, their application in regenerative medicine has drawn a significant attention. Aiming to address all the current challenges of aerogel as a potent scaffold in bone tissue engineering application, we adopted a novel synthesis approach to synergistically improve the pore size regime and mechanical strength in the aerogel. The 3D aerogel scaffold in this study has been synthesized through a versatile one-pot aqueous based sol-gel hybridization/assembly of organosilane (tetraethylorthosilicate, TEOS) and silk fibroin (SF) biopolymer followed by unidirectional

[*]**Corresponding author:** H.M: h.maleki@uni-koeln.de. [*]**Co-corresponding authors:** M.-A. S.: m.a.shahbazi@helsinki.fi.

Europe PMC Funders Author Manuscripts

freeze casting the as-prepared hybrid gel and supercritical drying. The developed ultra-light silica-SF aerogel hybrids demonstrated a hierarchically organized porous structure with interesting honeycomb shaped micromorphology and microstructural alignment (anisotropy) in varied length scales. The average macropore size of hybrid aerogel lied in ~ 0.5-18 μm and was systematically controlled with freeze-casting conditions. Together with high porosity (91-94%), high Young's modulus (~ 4-7 MPa, > 3 order of magnitude improvement compared to their pristine aerogel counterparts), and bone-type anisotropy in the mechanical compressive behaviour, the silica-SF hybrid aerogel of this study acted as a very competent scaffold for bone tissue formation. Namely, the results of *in vitro* assessments revealed that silica-SF aerogel is not only cytocompatible and non-hemolytic but also acted as an open porous microenvironment to trigger the osteoblast cells attachment, growth and proliferation on its surface within 14 days of incubation. Moreover, in order to support the *in vitro* results, *in vivo* bone formation within the aerogels implant in the bone defect site has been studied. The X-ray radiology and μ-CT analyses confirmed a significant new bone tissue density formed in the defect site within 25days of implantation. Also, *in vivo* toxicology studies showed a zero-toxic impact of aerogel implant on the blood biochemical and hematological parameters. Finally, the study clearly shows the potential of aerogel as a bioactive and osteoconductive open porous cellular matrix for successful osseointegration process.

Keywords

silica; silk fibroin; hybrid aerogel; sol-gel; bone tissue engineering

1 Introduction

Bone tissue engineering (BTE) is an alternative approach to current therapies available for severe bone defects with poor manifestations of self-regeneration1. Accomplishment of BTE needs three-dimensional (3D) templates (scaffolds) of appropriate morphology and chemical characteristics to imitate extracellular matrix (ECM) and allow cells to migrate, attach, grow, proliferate and differentiate2. A variety of materials, such as synthetic and natural polymers, ceramics, and hybrid materials as well as various manufacturing technologies have been employed to develop scaffolds with the aim of resembling physicomechanical and biological properties of bone tissue. Along with biocompatibility and biodegradability, an ideal scaffold for BTE needs a series of desires in terms of (micro)structural functions. Considering porous structure as an example, it is revealed that micron-size pores (20-1500 μm)3 are required for cell ingrowth, spreading and proliferation, while nanosized porous struts impart mechanical stability (desired is 5-10 MPa for compressive strength), flexibility, nutrition delivery, signaling communication of cells and excrements' removal4–5. In addition, hierarchically organized porosity is particularly advantageous for *in vivo* neovascularization and proper cell attachment across the scaffold. The large internal surface contributed by primarily micro and mesoporous struts also favors protein adsorption, ion exchange, and formation of the hydroxyapatite-rich cement line in the early stadium of osteoconduction6.

Silk fibroin (SF), a protein-based biopolymer with plenty of tissue-like features and high biocompatibility, controlled degradability, favorable mechanical strength, and processability to various material forms has been widely explored as the backbone of BTE scaffolds7–

8. Injectable gels9, freeze-dried9 or progene leached sponges9–10, electrospun11 and 3D printed constructs12–13, and composites with (bio) -inorganic materials14 are the most studied constructs of SF for cell colonization and proliferation *in vitro* and *in vivo*15. However, SF processing into ultralight and resilient aerogel, so-called *AeroSF*, with hierarchical porosity through successful implementation of sol-gel reaction and green supercritical CO_2 drying approach, has recently been reported in our group16. The reported *AeroSF* is hypothesized to become a potent biomaterial for the BTE as it provides improved mechanical feature and osteconductivity.

Aerogels are 3D porous nanostructured materials with exceptional physical properties, such as extremely low densities (0.003-0.5 g cm^{-3}), high specific surface areas (100-1200 m^2 g^{-1}), high porosities (80-99.9 %), and tunable surface and bulk chemistries17. Thanks to these promising features, they can be considered an interesting, supportive template for bone formation. However, the lack of micron-size porosity and poor mechanical strength combined with poor machinability or shaping to a sophisticated construct are still important bottlenecks, which should be mitigated in order to achieve a real breakthrough in aerogel mediated BTE6, 18. Therefore, further researches on aerogels are required to 1) develop robust processing techniques to confer controlled macroporosity to aerogel for host cell colonization, 2) improve the aerogel synthesis method to achieve a mechanically strong scaffold that can temporarily substitute natural tissues without compromising the biocompatibility of the materials and 3) allow the incorporation of bioactive compounds (*e.g.,* growth factor) in high yields to impart bioactivity to respective scaffolds and promote new tissue growth19–26.

For an efficient mechanical reinforcement in silica (SiO_2) aerogel, as a principal constituent of novel scaffold of current work, several strategies have been implemented16, 26–27. Among them, synthesis of mechanically robust hybrid aerogels with interpenetrating network (IPN) consist of sustainable biopolymers, such as polysaccharides and proteins to impart some mechanical resiliency to the delicate inorganic silica16, 27 and polysilsesquioxane (PMSQ, $[RSiO_{3/2}]_n$)28–29 structures has been drawn tremendous attention. We recently synthesized hybrid aerogels with IPN structure by combining the intriguing features of SF biopolymer with those peculiar physical properties in silica and silsesquioxane aerogels that reflect the properties of both initial constituents16, 30. Versatile *in-situ* sol-gel reaction of the SF solution with organosilane phase was conducted through precise control on the gelation kinetics and phase separation to form covalently bonded IPN structure at a molecular scale16, 28.

There are various ways in the literature to impart micron-sized porosity to the bone scaffolds31. Among the techniques like phase separation (soft) and template sacrification (hard), emulsion, and gas foaming, the unidirectional freeze-casting or ice templating method is turned out to function well1, 31. The unidirectional nucleation and growth of the ice crystals, as a green template, by applying a temperature gradient in the gel body not only provides the macroporosity but also renders the gel with a valuable bone type anisotropy or ordered honeycomb-like microstructure32. The anisotropic scaffold structure is further asset for the cell guidance, differentiation, bio-factor and nutrient transferring and the bone vessel formations within the final scaffold32–36. Also, the alignment of the microstructure in the

gel body toward the ice growth direction would not compromise the mechanical integrity in the scaffold as the other harsh, hard templating techniques do37.

Herein, we aim to develop a multi-scale porous hybrid silica-silk fibroin aerogels-based scaffold through *in-situ* processing of tetraethyl orthosilicate with SF biopolymer in an entirely aqueous based sol-gel reaction, followed by unidirectional freeze-casting followed by CO_2 supercritical drying ($scCO_2$) (Figure 1). In our proposed fabrication method, SF possesses high mechanical resiliency and supports the compressive and bending flexibility in the final scaffold as organic extracellular bony matrix. On the other hand, the nanostructured silica renders mechanical stiffness like inorganic reinforcement or filler as observed in bone. Moreover, proven osteoconductivity in nanostructured silica38–39 is speculated to equip the SF with bioactivity and cell adhesion feature, compensating the SF deficiency for arginine-glycine-aspartic acid (RGD) integrin, a peptide motif responsible for cell attachment to the ECM. Robust analogizing of the solgel reaction with unidirectional freeze casting could successfully improve the macroporosity, mechanical strength, and anisotropy in the microstructure with establishing a structure – properties relationship in the final aerogel scaffold. The final 3D composite scaffold was not only biocompatible but also highly osteoconductive and promoted new bone formation *in vitro* and *in vivo*.

2 Materials and Methods

2.1 Materials

All chemicals in this study were used without purification. The B. mori silkworm cocoons were purchased from Wild Fibers, UK. Tetraethylorthosilicate (98% purity, TEOS), hexadecyltrimethylammonium bromide (98% purity, CTAB), methanol (99.8%, MeOH), Ethanol (99.9%, EtOH), lithium bromide (LiBr) anhydrous, (99.99% purity, LiBr), sodium carbonate (Na_2CO_3), 4,5-Dimethyl-2-thiazolyl)-2,5-diphenyl-2H-tetrazolium bromide (MTT), Hoechst 33342, Dulbecco's modified eagle medium (DMEM), fetal bovine serum (FBS), Dulbecco’s Phosphate Buffered Saline (DPBS), trypsin, Triton X-100, ammonium molybdate tetrahydrate ($(NH_4)_6Mo_7O_{24}$), oxalic acid ($C_2H_2O_4$), 4-methylaminophenol sulphate, anhydrous sodium sulfite (Na_2SO_3), and sulphuric acid were received from Sigma-Aldrich. BCA-reagent A and slide-A-Lyzer Dialysis Cassettes with molecular weight cutoffs (MWCOs) of 3.5KD and a volume capacity of 3.5−5 mL were purchased from Thermo Fisher Scientific.

2.2 Silk fibroin extraction

The SF aqueous solution was extracted from silkworm cocoons through a slightly modified procedure reported in Nature Protocols by Kaplan *et al* 15. First, silk cocoons (5 g) were cut into dime-sized pieces and boiled for 30 min in a 2 L solution of Na_2CO_3 (0.02M); then fibers were rinsed with plenty of ultrapure water and dried overnight. The dry silk fibers were dissolved in LiBr (12−15 M) solution at 60°C for 4 h and then dialyzed against ultrapure water for 48 h. The dialyzed SF solution was centrifuged at 9000 rpm twice, and the supernatant was stored at 4°C for later use.

2.3 Preparation of unidirectional freeze-casted silica-SF aerogel hybrid scaffold

2.3.1 Preparation of silica-silk fibroin as-prepared gel—To obtain silica−SF composites, we adopted a one-step/one-pot acid-catalyzed sol-gel approach (*cf.* Figure 1) in which a sol with total volume of 5mL is prepared comprising organosilane (tetraethyl orthosilicate, TEOS, 3.37 mmol, 0.5 mL), SF biopolymer (4 mL, 4 wt/v%) in an aqueous acetic acid solvent (0.5 mL, 120mM), and CTAB (0.5 g). In the total sol mixture, the SF to silane mass fractions were 32:100. A homogeneous composite gel of silica-silk fibroin hybrid was formed in the ventilation oven (40°C) within 1 hour to complete the hydrolysis and condensation reaction of the silane phase and the sol-gel reaction at SF component, but also establishing some covalent and non-covalent interactions of both components at molecular state.

2.3.2 Preparation of silk fibroin as-prepared gel—SF based hydrogel was prepared according to our previous works16, 28 which is briefly explained in here. A mixture solution (5mL) of SF (4 mL, 4 wt/v %) and acetic acid (1 mL, 10 mM) was prepared. The solution was stirred for 15 min until a very low viscose gelly solution was obtained. Then the viscose solution was transferred to the PTFE mould to complete the gelation in a ventilation oven (40 °C, 4 hrs).

2.3.3 Unidirectional freeze-casting or ice templating the as-prepared silica-SF gel—The as-prepared weak hydrogels with interpenetrating network have been undergone to the unidirectional freeze-casting according to the modified procedure reported by Nishihara *et al.*40 Freeze-casting was performed through immersing the cylindrical gel unidirectionally at a constant rate of V_f (33 and 66 cm h^{-1}) into a cold bath maintained at a constant temperature of T_f (-10 and -197°C). The resulted sample has been designated as silica-SF-T_f-V_f at Table 1. The ice growth was initiated from the bottom of the tube and continued until the tube was completely frozen. Afterwards, the sample was transferred into a cold bath maintained at 0°C for 2 h in order to preserve the ice rods template in the gel to strengthen the structure and preserve the created semi-microhoneycomb shaped structural pattern. After this low-temperature aging, the sample was thawed at room temperature, 23°C for 0.5 h. The Thawed samples were transferred into the oven at 40°C for 48 h in order to continue aging and allow finalization of the rest of the sol-gel reaction in the gel. Next, sample were washed four times with 8 h interval with ethanol to remove CTAB and unreacted precursors and treated with 70:30 (v/v) methanol: ethanol mixture and finally transferred into $scCO_2$ autoclave and supercritically dried.

The same directional freeze-casting approach was also applied for SF based hydrogel.

2.4 Chemical, biophysical and mechanical properties of the aerogel

Solid-state ^{29}Si and ^{1}H NMR spectra of the aerogels were obtained by using an Inova 500 spectrometer using a 4 mm solids probe with cross-polarization and magic angle spinning at 11 kHz. A solid-state $^{1}H–^{29}Si$ heteronuclear correlation NMR spectrum was collected using 4 mm zirconia rotors with a spinning rate of 11 kHz and applying homonuclear decoupling using continuous phase modulation (DUMBO) to increase the ^{1}H spectral resolution. TEM images were recorded with a JEOL 200F cold field-emission (W) filament,

200 keV operated at an accelerating voltage of 300 kV. EDS-TEM elemental mappings were recorded by JEOL, Centurio 100, detector area of 100 mm, the solid angle of 0.97sr, and resolution of ~ 133 eV for Mn. Scanning electron microscopy (SEM) images were taken with a scanning electron microscope (Zeiss ULTRA Plus) running at 5 kV with an in-lens detector and a working distance around 4 mm. SEM-EDX spectra were taken by the same microscope running at 15 kV and a working distance around 9 mm. For x-ray microcomputed tomography data, the sample scanned with RX solutions (EasyTom 160) using a 4032×2688 CCD camera (Ximea, Germany) and a LaB_6 filament working at voltage: 50kV, current: 90uA, integration time: 750ms averaging: 6, projections: 3488. The bulk density was calculated from the corresponding mass and volume of the cylindrical aerogel. Nitrogen adsorption-desorption measurements were carried out at 77 K using a Micrometrics ASAP 2420. Before analysis, the sample was outgassed at 60 °C in vacuum (10−5 bar) for 24 h to remove adsorbed species. The skeletal density was measured using a helium pycnometer (AccuPyc II 1340, Micromeritics, USA). From the skeleton and bulk densities values, the porosity ε (%) (1), pore volume (V_p) (2), and pore diameter (D_p) (3) of the samples were calculated according to equation given at below

$$\text{Porosity, } \varepsilon\,(\%) = \frac{1/\rho_b - 1/\rho_s}{1/\rho_b} \times 100 \tag{1}$$

$$\text{Pore volume, } V_{pore}(cm^3\,g^{-1}) = (1/\rho_b - 1/\rho_s) \tag{2}$$

$$\text{Pore diameter, } D_{pore}(nm) = 4V_p/S_{BET} \tag{3}$$

The specific surface area was calculated with the Brunauer, Emmett, and Teller 5-point method in the relative pressure range of 0.05−0.3. Mechanical characterization of the composites was carried out on the monolithic cylindrical samples using a universal mechanical testing equipment (Zwick/Z010, Zwick/Roell, Germany) equipped with a 1 kN force transducer (KAP-S, AST Gruppe GmbH, Germany) in a controlled environment (23 °C, 50%).

2.5 Cell lines, culture conditions, and scaffold preparation conditions

The human osteosarcoma MG-63 cell line (ATCC CRL-1427) was cultured in DMEM supplemented with fetal calf serum (10% FBS), 100 U/ml penicillin and 0.1 mg/ml streptomycin. The cultures were maintained in a humidified incubator at 37°C with 5% CO_2.

The aerogel scaffolds (6 mm diameter X 1 cm height) were treated with graded ethanol (100%, 70%, 50% and 20%, 30 min each treatment) to sterilize them. The marixes were then

washed with excess 1 X Dulbecco's phosphate buffer saline (DPBS) (pH 7.4) 3 times, 15 min each for complete removal of the ethanol. After washing, the sterilized aerogel scaffold was incubated in complete culture media to precondition them for boosting cell attachment and biocompatibility test. For cell seeding test, the excess media was removed by squeezing the scaffold very gently prior to cell seeding in order to soak the cell suspension without letting them to float around.

2.6 Cell viability

Indirect MTT assay was performed in order to test the cytotoxicity of scaffold's degradation or leaching products for 14 days. Prior to the test, the sterilized aerogel scaffolds were immersed in DMEM + 10% FBS and antibiotics for each time point (5 time points, 3 replications) at 37 °C in 5% CO_2. Also, blank medium (negative control) was incubated in the same condition for 14 days. 100 μl with 30,000 cells were seeded in fresh DMEM + 10% FBS in each well in 96-well plate for 24 h. At each time point (day 1, 3, 7, 10 and 14) the medium of each well, containing cells, was exchanged with 100 μl of scaffold's, blank or fresh medium (DMEM + 10% FBS) and incubated for 48 h. Afterwards, MTT staining solution (10 μl, 5 mg/ml in DPBS) was added to the cell culture medium of sample, negative control, and fresh medium and incubated for 1.5 h at 37°C. Next, the MTT solution was discarded, and 100 μl of isopropanol was added to lyse the cells. After 5 min of shaking, the absorption at 565 nm was measured on a TECAN Infinite m200 pro microplate reader.

2.7 Visualization of cellular attachment

The cell morphology and attachment on aerogel scaffold was tested by scanning electron microscopy (SEM) and inverted fluorescence microscopy (Olympus IX70). The sterilized aerogel samples were put in 48-well plates. 500 000 cells were then counted and added to each well followed by medium replacement every 48 h. At each time point (day 1, 3, 7 and 14), the samples were taken out of the culture medium, washed with DPBS (pH 7.4) three times and fixed by 2.5% glutaraldehyde (in DPBS) at 37 °C for 1 h. After that, the samples were dehydrated with different concentrations of ethanol (50, 70, 96 and 100%) and finally vacuum-dried. The dried aerogel samples were then sputtered with gold and analyzed with SEM. For fluorescence microscopy, the DNA of fixed cells attached to the scaffold was stained with Hoechst 33342 (10 μg/ml in DMEM) and incubated for 15 min at 37°C in dark. Afterwards, the samples were washed twice with DPBS and cell nuclei were visualized by fluorescence microscopy.

2.8 Hemolysis assay

Fresh human blood samples stabilized by heparin were obtained from anonymous donors with the permission of the respective institutional ethical committee. Within 2 h after blood sampling, red blood cells (RBCs) were isolated by mixing 5 mL of blood with 10 mL of DPBS and centrifugation at 2500 rpm for 6 min. This step was five times repeated to obtain a RBC pellet. Next, 5 % hematocrit suspension was obtained by mixing 1 mL of the RBCs pellet with 19 mL of DPBS. The hemolytic effect of the scaffold was investigated by adding 200 μL of the 5 % hematocrit to 800 μL of the different concentrations of scaffold powder in D-PBS to reach the final concentrations of 100, 200, 400, 800, and 1200 μg/mL. Each of the samples was vortexed for 5 sec and subsequently incubated at room

temperature for 2, 4, 8, and 24 h. In each time point, the samples were gently vortexed for 5 sec and centrifuged at 13000 rpm for 3 min. Afterwards, 100 μL of the supernatant was withdrawn to 96-well plates (Corning Inc. Life Sciences, USA), followed by quantification of the lysed hemoglobin at 577 nm using a Varioskan Flash Multimode Microplate Reader (Thermo Fisher Scientific Inc., USA). Milli-Q water were used as positive controls with 100 % of RBC lysis effect. The results represent the average of, at least, three independent experiments.

2.9 *In vivo* radiography, μ-CT analysis and toxicity assessment during bone formation

The animal experiments were approved by the Animal Ethical Committee of Zanjan University of Medical Sciences. The osteogenic support of the developed scaffold was studied on healthy Sprague Dawley male rats weighing 310-335 g. Fifteen rats were equally divided to three groups. The first group was control without any bone defect and scaffold implantation. The other two groups were 1) animals with bone defect induction in the femur but without scaffold implantation, and 2) animals with bone defect induction in the femur and scaffold implantation. Bone defects were similar in all animals, and the scaffolds were implanted at the defect site by press-fit method for 25-day monitoring of the bone formation and 60-day toxicity assessment. For radiological and μ-CT analysis (Phoenix vjtomejx s, GE, Germany), the animals were euthanized, and femurs were removed from all the 3 groups and subjected to the radiological and μ-CT experimentations. Macroscopic photos of regenerated sites were also taken in 25 days post-implantation. These studies were performed to investigate the regeneration of bone and tissue ingrowth, position of the implant inside bone, and scaffold interaction with the host bone over the wound closure time. The X-ray imaging was under the condition of 75 mA, 85 kV, 500 msec/slice, and voxel size 26 mm. For the *in vivo* toxicity test, blood collection from the animals was performed after 1, 15, 30, 45, and 60 days of scaffold implantation for the analysis of the different biochemical and hematological parameters. The blood analysis was performed within 4 h post-sampling, and the plasma biochemistry studies were conducted on the same day of the blood collection. In all *in vivo* studies, all animals were kept at ventilated temperature-controlled animal room five days before starting the experiments. The relative humidity of 60 ± 10% and a 12-h light/dark daily cycle were applied in the animal room. During the studies, standard polycarbonate stainless steel wire-topped cages were used for housing the animals and free access to rat chow and water ad libitum were provided.

2.10 Statistical analysis

The results are expressed as mean ± standard deviations (S.D.) of at least three independent set of measurements. Statistical analysis was achieved by means of oneway and two-way analysis of variance (ANOVA) with the level of significance set at probabilities of *$p < 0.05$, **$p < 0.01$, and ***$p < 0.001$, analyzed with GraphPad Prism 7 software.

3 Results and discussions

3.1 Physical, microstructural, and mechanical characteristics of the scaffold

In this study, the *in-situ* acid catalyzed sol-gel reaction associated with unidirectional freeze-casting approach has been implemented on the silica-SF gel for producing anisotropic

multiscale porous aerogels. According to Figure 1, when silica-SF hybrid hydrogels, which are freshly gelled and have an enough amount of solid phase, are frozen unidirectionally under a pseudo-steady-state of ice growth condition, an array of phase separated polygonal ice rods grow in parallel with the freezing direction from the bottom of gel. This strategy produces frozen gel consisting of anisotropic ice crystals surrounded by the walls formed the dispersed silica nanoparticles and SF fibers (Figure 1). After removal of the ice template and supercritical drying, monolithic aerogel with almost ordered macropores can be obtained. In the literature, the unidirectional freeze-casting which uses the ice as structural directing agent has been referred as Ice Segregation Induced Self Assembly (ISISA)32, 40 process which form an anisotropic structure from sol, gel and various type of slurries like polymer and nanosheets.

According to Table 1, beside sol-gel reaction parameters, the freezing conditions have also a high control on the micromorphology of the resulted gel such as pore orientation, size and other physical properties such as the extent of the porosity ε (%), specific surface area (S_{BET}) and mesopore size regime (D_{pore}). The gel obtained by low cooling rate (33 cm h^{-1}) and low cooling temperature (-196°C, LN_2), silica-SF-196-33, has shown bigger macro- size pores (17.84 ± 2.75) compared to that obtained with high cooling rate (66 cm h^{-1}) and high freezing temperature (-10°C), silica-SF-10-66 (0.52 ± 0.14) (*cf.* Figure S1). This finding is in agreement with the work of Nishihara *et al.*40 who developed silica gel with an ordered macroporous honeycomb-like microstructure with an average macropore size range of 3 to 40 μm under varying freezing conditions. According to their finding, in the lower freezing temperature (T_f) and the lower immersion rate of the gel into the cooling bath (V_f), the bigger macropores in the gel body could be obtained40.

Also, all freeze-casted aerogels have indicated a high extent of porosities (91-94%) with bulk densities (ρ_b) and Yong's modulus (ε) highly dependent on the freezing direction (*cf.* Table 1).

The silica-SF-196-33 was the lightest (ρ_b=0.075 g cm^{-3}) and the strongest hybrid scaffold (ε=7.3 MPa) as seen from data at Table 1 and the stress-strain curve obtained by compressive studies (See also Figure S2). The reported bulk density in silica-SF-196-33 are also lower than that of previously reported open-cell scaffold foams or sponges41. In this aerogel, it is hypothesized that the microstructural alignment caused by unidirectional freezing the gel has provided a strength toward compressive loads.

Therefore, the silica-SF-196-33 aerogel scaffold, hereafter denoted as ‘’silica-SF aerogel scaffold” has been selected as aerogel with optimal structural and mechanical properties and implemented detailed characterizations and biological studies.

The internal microstructural pattern, from a multi-scale standpoint, has been studied with a combination of scanning electron microscopy (SEM), transmission electron microscopy (TEM) and X-ray microtomography (μ-CT) for the silica-SF-196-33 aerogel (Figure 2a–c). Figure 2a revealed aligned polygonal pores with a diameter of ~18 μm (measured by ImageJ) and a cell wall thickness of 0.4 – 1.5 μm (Figure 2a, T-Section). Since the aligned macropores have a polygonal cross-section and are parallel to the freezing direction (Fig 2a,

L-Section), we named this micromorphology of the obtained material as microhoneycomb because it resembles miniaturized honeycomb topological structure42.

The microstructural alignment is also notable at low length scale (nanometer) as shown in Figure 2b, with uniform distribution of all key network elements Si, C, N, O as observed with TEM-EDX elemental mapping (Figure 2d). μ-CT analysis at Figure 2c revealed that the pores are developed as millimeter-long rode parallel to the freezing direction throughout the material. Cross-sections taken at different positions along the ice growth direction show that the pore density is almost the same in all lengths of the sample. However, the pore size slightly decreases toward the center of the material which could be possibly due to the low thermal contact of gel center with the ice bath. This suggests that the pore structure is almost uniform with relatively moderate extent of pore interconnectivity. The detailed visual observations of the 3D scaffold structure are presented in the supplementary information (Video S1–2).

The stress-strain curves in Figure 3a display the typical deformation behavior of freeze casted aerogels, that is, linear elastic behaviour at low strain followed by a successive pore collapse-related stress reduction at intermediate strains, and finally a plastic yielding plateau with subsequent strain hardening at high strain. We obtain a Young's modulus of $\varepsilon = 7.3$ MPa along the pore (freezing) direction (Figure 3a, axial) which is significantly higher than the values for previously reported pristine silk fibroin (0.09 MPa)16 and silica aerogels (5–20 kPa)43 and comparable with that of recently reported silk fibroin/carbon nanofiber composite (~ 10 MPa)44. This anisotropic mechanical behavior in the scaffolds resemble the anisotropic structure of bone that is often stronger in the direction with high mechanical load.

3.2 Scaffolds chemical characteristics

The one pot gelation of the SF biopolymer with (organo)-silane is occurring in two steps. First, gelation is induced by assembling the SF in diluted acidic media. The silk fibroin proteins become physically cross-linked/ assembled followed by simultaneous hydrolysis and polycondensation of the (organo)-silanes in a second step (*cf.* Figure 1). However, based on our previous studies, *in-situ* assembly of SF with silanes is very sensitive to the type of the silane precursor as well as to the gelation pH. Processing of the SF with methyltrimethoxy silane ($CH_3Si(OCH_3)_3$, MTMS)28 precursor resulted in superhydrophobic final materials which whose gelation was hardly controlled due to the polarity differences in sol components as well as in the gelation kinetics of organic and inorganic phases. Although these issues were solved by adding a phase separation suppressing agent to the sol mixture as well as conducting the gelation process in a successive two-step process, the superhydrophobicity of the resulted hybrid aerogel still hindered its application in biological environments.

By using tetrafunctional silanes like tetramethylorthosilicate ($Si(OCH_3)_4$, TMOS)16, 30, as a silane source of hybrid, the macroscopic phase separation during the gelation has been significantly circumvented. But the methanol byproducts released from the hydrolysis and condensation reaction caused an α helix- to- β-sheet transformation in the SF component of gel and subsequently caused a shrunk, stiff and hardly degradable final hybrid gel product16.

The stiffness in this hybrid aerogel was avoided using the silane coupling agents $(OR)_3Si\text{-}R'$. In this case, the coupling agent has not only mediated the covalent interactions between SF and silica but also increased the mechanical resiliency of the gel due to the presence of flexible R' groups. Nevertheless, the presence of non-hydrolysable -Si-C bond45, also known as a non-degradable bond, in the formed gel structure was still problematic for BTE applications. In this study, one step sol-gel processing of tetraethylorthosilicate ($Si(OCH_2CH_3)_4$, TEOS) with SF in the presence of acid catalyst (acetic acid), and minute amount of surfactant, CTAB, as a phase separation suppressing agent, appears to be more appealing. As with later, the polarity difference in the gel components and subsequent precursors' demixing in the aqueous phase has been substantially circumvented. This is also evident from homogenous (molecularly) distribution of network elements in the TEM-elemental mapping as shown at Figure 2d. Importantly, the resulted final gel has very good structural stability in the aqueous and cell media (*cf.* Figure 1) with very slow disintegration rate.

SF sol-gel transition occurs through inter, intrachain hydrogen bonding or physical-crosslinking between the peptide chains in the presence of the acid catalyst46. During the gelation, some of the α-helix structures in the SF polymer chains will also partially be transformed into the β-secondary crystalline structure as a mechanically more stable conformation, and therefore toughen the obtained gel46. Due to the availability of abundant various functional groups in the SF, silica phase is incorporated into the SF network in different ways. A typical example might be based on covalent bonds, hydrogen bonding and/ or dipole-dipole interactions (*cf.* Figure 3)28. The more probable covalent interactions, as seen in solid-state MAS ^1H NMR spectrum at Figure 3b, is through condensation of abundant surface silanol groups –(Si-OH) with dangling hydroxyl functionalities of the SF network (*e.g.,* with serine amino acids) to form ≡Si−O−**CH_2-(Ser)**, δ: 3.3 ppm. On the other hand, the silane sol-gel polymerization in the sol mixture is followed simultaneously by formation of different condensed silica species designated at ^{29}Si CP-MAS NMR spectroscopy, Figure 3c, as Q_n peaks, Q_4, (δ: −110 ppm), Q_3, (δ: −99 ppm), and Q_2 (δ: −91 ppm), where n is the number of ≡Si−O−Si≡ bridges. During the silane gelation, a network of particles forms which is "glued" together by the secondary phase of the silk fibroin network and therefore forms an interpenetrated network of silica-SF16. Thermogravimetric analysis as shown in Figure 3d indicates that the silica−SF aerogel hybrids are thermally stable up to ~253 °C which relatively similar to the other aerogel composites obtained with other biopolymers like pectin and cellulose27, 29. SF and the non-reacted ethoxy moieties in the network decompose around 253 and 395 °C, respectively, being the SF polymer comprised 22% of the overall mass of the aerogel scaffold.

The ^1H-^{29}Si heteronuclear correlation (HETCOR) MAS NMR technique at Figure 4, confirms the appropriate molecular proximity of network constituents, SF, and silica in the hybrid structure through the coupling of SF protons with Si atoms. The correlation of methylene protons in the side chain of SF network (serine and threonine, $-CH_2OH$, ^1H NMR) with silicon atoms (Q_4, Q_3, ^{29}Si NMR) of the silica network shows cross-peaks that further reflects the formation of molecularly mixed SF and silica domains instead of formation of separated individual SF and silica enriched domains in the composites.

This kind of correlation were also observed in our previous studies with the other silane phases (TMOS and MTMS) co-gelled with SF polymer16, 27–28. In general, this technique provides a broad view regarding the homogenous molecular scale mixing of the SF with silica/silsesquioxane phases regardless of covalent or non-covalent interactions27.

3.3 Silica-SF aerogel scaffold biological properties (*in vitro*): cell viability, attachment, and morphology, protein adsorption, hemocompatibility, biodegradability and biomineralization studies

Cell viability—The 14 days MTT assay study shows that silica-SF aerogel scaffold extracted medium possesses minimum cytotoxicity against osteoblast cells, which was comparable to those of control and the blank mediums (Figure 5a). The medium collected from the incubated scaffold's degradation product not only didn't cause any toxicity but also, the growth and proliferation of osteoblasts on day 7 and day 10 were even better than that in negative control and fresh medium. This suggests that the degradation or leaching product of the scaffold was not only non-toxic but also increases the proliferation and growth of osteoblasts compared to the blank medium.

Protein adsorption—In tissue engineering, the adsorbed proteins on the scaffold or implant surface are the crucial regulator of many key signalling pathways. Namely adsorbed protein can give signals to the cells' integrin and boost cell adhesion to the scaffolds' surface47. Adsorption of the FBS on the silica-SF aerogel scaffold surface was investigated at three-time points of 3, 8 and 24h with BCA assay to quantify the amount of the adsorbed protein. As it is seen from Figure 6b, the initial average protein adsorbed on aerogel surface is high (400 μg/mL, 3 h), which then slightly increased to 430 μg/mL after 8h of incubation and subsequently dropped to 370 μg/mL after 24 h. The extent of the protein-biomaterial interaction is largely defined by the pore structure, surface charge and surface roughness44. The dual meso-macroporous character in aerogel scaffold associated with high internal surface area (S_{BET}=433 m^2 g^{-1}) render their surface highly prone to FBS protein adsorption47. In the other hand, we expect overall positive surface charge for synthesized silica-SF aerogel due to the used acid catalyst in the sol-gel reaction which further augmented the adsorption of negatively charged BSA proteins of FBS. However, for 24 h, due to the slight surface erosion of the scaffold upon degradation, the protein adsorption was slightly declined.

Hemocompatibility—The acceptance of the whole biomaterials by the host tissue without provoking any adverse or undesirable effect, *e.g.* without lysing of the red blood cells is also known as biocompatibility48. Silica-SF aerogel matrix causes minute amount of hemolysis (*cf.* Figure 5c). The level lies at the range of non-hemolytic to slightly hemolytic (<2 to 2-8%) according to the standard hemolytic index (ASTM F756-00(2000))44. Our hemolysis data imply that the silica-SF aerogel is clinically implantable due to minimal effect on the lysis of RBCs, which can cause the release of pro-coagulant factors and consequently affect the blood flow and induce thrombogenesis49.

Biodegradation—Biodegradability within an acceptable time without the release of any harmful metabolic product is one of the most important features of biomaterials as it enables

incremental replacement of the scaffolding material by newly formed functional tissue. The biodegradation rate of a biomaterial depends largely on its composition and 3D structure50. Since silica-SF aerogel scaffold is highly porous (94%), thus aids the enzyme to access to the internal structure and facilitates its biosorbability. The degradability of SF component of scaffold was monitored through incubation of scaffold with PBS and PK (proteolytic enzyme) solutions under a slight agitation (100 rpm, 37°C) and by monitoring the scaffold overall weight loss in scaffold at each time point. Simultaneously, the degradation of silica into the silica species, *e.g.* silicic acids, $Si(OH)_4$, in the PBS and PK supernatants for each time point were also studied through silicomolybdic acid (SMA) spectrophotometric method (*cf.* Figure 5d (*i*) & (*ii*)). The SMA method allows to monitor the presence of monomeric silicic acids through formation of blue heteropoly acid, silico-12-molybdic acid, ($H_4SiMo_{12}O_{40}$ *cf.* Figure 5d *(ii)*) complex which has an absorbance band in λ=810 nm. As it is shown in Figure 5d *(i)*, an intensity increase in the UV-Vis spectra can be visually confirmed with an increase in the colour intensity of blue SMA complex at higher incubation times. Particularly, the intensity of blue complex colour is proportional to the concentration of degraded silicate species in the solution. For 14 days of incubation, 0.22 % of silica is degraded in PBS, but a lower degradation quantity (0.18%) is observed in case of PK due to the possibility of interaction of enzyme with molybdate reagent which prevented SMA complex formation. Instead, in 14 days, SF degradation in PK (8% degradation) is higher than that observed in PBS solution (2.7% degradation) (cf. Figure 5d (*iii*)). Previous studies showed that *b. Mori* scaffold sponges degraded quite faster (within one month) leaving the gap early without the formation of the neo-tissue51. The hybridization of SF with silica seems to contract high degradability of SF and keeps the balance between the scaffold degradation and *in vivo* new tissue formations. The fate of these released degradation products may follow two paths: either remain in local tissue or degraded with alveolar macrophage44.

Biomineralization—The bone-like hydroxyapatite (HAp, $Ca_{10}(PO_4)_6(OH)_2$) crystal formation on the scaffold surface was confirmed with XRD diffractogram at Figure 5e for different immersion times in the simulated body fluid (SBF). Except the peaks masked by broad characteristic peak of silk fibroin at 21° and 24°, the characteristic peaks at 26.5° (0,0,2), 31.9° (2,1,1), 45.5° (2,2,2) and 56.6° (3,2,2)44 significantly match with the standard HAp crystallographic planes enlisted in JCPDS card number 09-0432. These results are in line with our observation in SEM study at Figure S3 and confirm the ability of our fabricated conductive silica-SF aerogel scaffold to form apatite in a short time period. The SEM images show a significant change in micromorphology of the scaffold matrixes with respect to the plain scaffold (Figure 2a), where different amount and the size of Ca-P salts are formed with immersion in SBF. Also, SEM micrographs revealed significant changes in the morphology of HAp from small aggregate of particles (3^{rd} days) to micrometric sized clusters of Ca-P crystals in the higher incubation time (14^{th} days). The elemental composition analyzed by EDAX (Figure S3) are also found to be similar with the stoichiometric ratio of HAp crystals.

The formation of Ca-P crystals indicates the surface bioactivity of silica-SF scaffolds and its ability to absorb $PO4^{3-}$and Ca^{2+} electrostatically. The surface silanol groups of nanostructured silica in the scaffold can attract Ca2+ cations of SBF and create a surface

layer with positive charge, which can then adsorb $PO_4^{3-}$and make the apatite to nucleate and grow.

Cell attachment, ALP activity and mineralization assessment—It is already known that the osteoblast is highly receptive to the surface chemistry, roughness and energy of the materials. It is expected that highly porous character and the presence of the nanostructured silica together with SF fibrous nature ultimately increase the surface topography and therefore increase the cellular interaction. On the other hand, as the SF in the scaffold tended to swell in the medium, (swelling ratio: 22.1 % after 24h) the structure became bigger in size and the cells inclined into the scaffolds. Therefore, as can be seen from SEM micrographs and fluorescence images of Hoechst 33342 stained attached cells (*cf.* Figure 6a-d), silica-SF aerogel supports the osteoblast cell growth and proliferation up to 14 days. On day 1, cells started to attach to the aerogel scaffold surface with almost the same morphology as seen on the surface of coverslips, as a reference, and the scaffold microstructure is quite different than what is observed in plain scaffold (see also Figure 2a). On day 7, it seems that the cellular actin filament substantially covers the surface of the scaffold with an increase in the cell-to-cell contact through cytoskeleton extension and occupies the interconnected 3D pores (see arrowheads in Figure 6c). On day 14, a confluent cell layer with rough surface covered the entire surface of silica-SF aerogel scaffold reflecting multilayer proliferation of MG-63 cells forming a uniform and compact ECM on the silica-SF aerogel.

As the early marker of bone cell differentiation, Figure 6e shows the ALP activity of cells cultured on the scaffold and TCP. At day 1, both groups demonstrated very low ALP activity, which represents poor differentiation of the cells into the osteoblast phenotype. Measurement of the ALP activity in the next days showed significantly higher ALP activity for the MG-63 cells seeded on the scaffolds than the blank TCP at each time point. In addition, mineralization was evaluated by the determination of calcium content, known as the late marker of cell differentiation toward osteoblasts. In line with ALP activity test, Figure 6f shows remarkably higher deposition of calcium on cells at day 7 and 14 for the scaffolds compared to TCP samples. These findings imply that the silica-SF aerogel scaffold, which possesses the main constituent of human bones, can provide outstanding biomimic environment for the attachment of osteoblast cells as well as growth, proliferation, osteogenic differentiation, mineralization and eventually osteogenesis for bone formation within a short time period.

3.4 *In vivo* studies

The main purpose of tissue engineering studies is to regenerate the structure and function of damaged tissues through the systematic trigger of molecular signalling of involved cells. A soft or hard three-dimensional structure made of degradable biomaterials is usually applied to provide a temporary template for cell proliferation *in vivo*52. Therefore, we investigated *in vivo* bone formation potential of the fabricated 3D silica-SF aerogel scaffold by the macroscopic optical imaging, as well as X-ray and μ-CT studies53–54. The macroscopic images showed the new bone formation around and inside the implants (Figure 7a). Biocompatibility of the scaffold was approved since macroscopic degenerative change and

necrosis were not observed in the defect site and around the boundary of the implanted scaffold at 25-day post-implantation. Sabri *et al.* 55–56 have also previosly substatiated the biocompatibility of multichannel silica based aerogel hybrid as pripheral nerve repair scaffold in the rat model. In contrary, necrosis and cellular degeneration was observed in the animals that did not receive post-surgical scaffold implantation in the defect site of the femur. The images of the scaffold receiving group also showed the integration of the scaffold into bone microstructure during the study period without any harmful effect on the surrounding tissues. In fact, the scaffold was well accepted by the local bone tissue without complications, such as infection, bleeding or inflammation. In line with optical photographs, μ-CT imaging exhibited the desirable progression of the bone tissue regeneration in the scaffold inserted animals (Figure 7b). The periosteum formation was complete in the animals receiving scaffold implantation, but very poor growth of periosteum was observed in the defect site of scaffold-free group. The X-ray radiography images showed a remarkable difference in the radiodensity of the defect site in surgery/no scaffold and surgery/scaffold animal groups, which proves the successful scaffold mediated bone formation and favorable host-material interaction. The counterplot colour-based bone density analysis of the radiography images demonstrated green areas in the red healthy and dense tissues of the bone, a sign of remained bone defect after 25 days post-surgery in the animals that did not receive scaffold implantation (Figure 7c). On the other hand, as an indicator of the mineralized callus synthesis and bone healing, the defect area of the bone was showing red colour and there was no sign of low-density bone (green colour) in the scaffold implanted animals. The corresponding bone density profiles of the black line shown in the counterplot colour-based images of each group of the animals are also shown. The bone density of the scaffold implanted area is similar to intact bone of the control group after 25 days, confirming rapid initiation of new and healthy bone formation.

A detailed examination of the *in vivo* toxicology of the scaffold was further performed over sixty days to identify its *in vivo* translation potential. Sixteen biochemical and hematological parameters were screened (*cf.* Figure 8). It was found that no meaningful changes were observed in red blood cells (RBC), hemoglobin (HGB), hematocrit (HCT), and platelet (PLT) level for the scaffold implanted group in comparison to the control group (Figure 8). On the other hand, the number of white blood cells (WBC) was increased. Since no infection was observed in the animals at the site of surgery, the increased values for WBCs can be associated with the inflammation and intelligent immunity due to the surgery performed on the animals that received scaffold implantation. A series of blood biochemical indexes and minerals, including blood urea nitrogen (BUN), creatinine (CREA), lactate dehydrogenase (LDH), alkaline phosphatase (ALP), total protein (TP), albumin (ALB), calcium (Ca), and phosphor (Ph) were examined. Among all, just ALP and ALB demonstrated significant abnormity comparison to the control group. As functional indexes for the proper function of organs in the body of mice, other factors showed negligible changes between control and scaffold implanted groups. In general, we concluded that the tested scaffold does not have a negative impact on hematological, renal and hepatic function of the animals.

4 Conclusions

Hierarchically organized porous silica-silk fibroin aerogel hybrids with honeycomb like macropore morphology has been synthesized through a novel aqueous based sol-gel process, unidirectional freeze-casting and supercritical drying approaches. The hybrid aerogel of this study demonstrated a multitude of improved properties such as high porosity, high specific surface area with an interesting anisotropic micromorphology and improved anisotropic mechanical behavior. The *in vitro* cell biology experiments within 14 days of incubation revealed that aerogel scaffolds are biocompatible, and their surface is very prone to the osteoblast attachment and growth. In addition, due to the high specific surface area originating from their micro and mesoporous microarchitecture, as well as the osteoconductive nature of nanostructured silica component in the scaffold, the surface of scaffold augmented the protein adsorption as well as the sedimentation of bone type hydroxyapatite minerals, respectively. The *in vivo* bone formation studies supported the *in vitro* studies and substantiated the high potential of aerogel implant to support the new bone tissue in the defect side without any negative biochemical and hematological toxic effects during bone formation. Finally, the fruitful biophysical and biological characteristics of the present aerogel composite may help in mimicking the *in vivo* physiological niche as well as *in vitro* bone disease tissue models.

Supplementary material

Refer to Web version on PubMed Central for supplementary material.

Acknowledgments

The synthesis part of this paper was conducted under the framework of Austrian Science Fund-(FWF) Lise-Meitner fellowship (project no. M2086-N34). at University of Salzburg, Department of Chemistry and Physics of Materials. Therefore H.M. acknowledges financial support by the FWF. S.M. acknowledges financial support from Interreg Österreich−Bayern 2014-2010 Project AB29Synthese, Charakterisierung und technologische Fertigungsansätze für den Leichtbau“n2m”(nano-to-macro).

References

(1). Melke J, Midha S, Ghosh S, Ito K, Hofmann S. Silk Fibroin as Biomaterial for Bone Tissue Engineering. Acta Biomater. 2016; 31: 1–16. [PubMed: 26360593]

(2). Hutmacher, DW. Advanced Manufacturing Technology for Medical Applications : Reverse Engineering, Software Conversion and Rapid Prototyping. Gibson, I, editor. Vol. Chapter 8. John Wiley & Sons, Ltd; 2005.

(3). Murphy CM, O'Brien FJ. Understanding the Effect of Mean Pore Size on Cell Activity in Collagen-Glycosaminoglycan Scaffolds. Cell adhes migr. 2010; 4: 377–381. DOI: 10.4161/cam.4.3.11747 [PubMed: 20421733]

(4). Karageorgiou V, Kaplan D. Porosity of 3D Biomaterial Scaffolds and Osteogenesis. Biomaterials. 2005; 26: 5474–5491. [PubMed: 15860204]

(5). Pircher N, Fischhuber D, Carbajal L, Strauß C, Nedelec J-M, Kasper C, Rosenau T, Liebner F. Preparation and Reinforcement of Dual-Porous Biocompatible Cellulose Scaffolds for Tissue Engineering. Macromol Mater Eng. 2015; 300: 911–924. DOI: 10.1002/mame.201500048 [PubMed: 26941565]

(6). Maleki H, Durães L, García-González CA, del Gaudio P, Portugal A, Mahmoudi M. Synthesis and Biomedical Applications of Aerogels: Possibilities and Challenges. Adv Colloid Interface Sci. 2016; 236: 1–27. [PubMed: 27321857]

(7). Murphy AR, Kaplan DL. Biomedical Applications of Chemically-Modified Silk Fibroin. J Mater Chem. 2009; 19: 6443–6450. DOI: 10.1039/b905802h [PubMed: 20161439]

(8). Ding Z, Han H, Fan Z, Lu H, Sang Y, Yao Y, Cheng Q, Lu Q, Kaplan DL. Nanoscale Silk–Hydroxyapatite Hydrogels for Injectable Bone Biomaterials. ACS Appl Mater Interfaces. 2017; 9: 16913–16921. [PubMed: 28471165]

(9). Oliveira AL, Sun L, Kim HJ, Hu X, Rice W, Kluge J, Reis RL, Kaplan DL. Aligned Silk-based 3-D Architectures for Contact Guidance in Tissue Engineering. Acta biomater. 2012; 8: 1530–1542. DOI: 10.1016/j.actbio.2011.12.015 [PubMed: 22202909]

(10). Kim U-J, Park J, Joo Kim H, Wada M, Kaplan DL. Three-dimensional Aqueous-Derived Biomaterial Scaffolds from Silk Fibroin. Biomaterials. 2005; 26: 2775–2785. [PubMed: 15585282]

(11). Ki C-S, Park SY, Kim HJ, Jung H-M, Woo K-M, Lee J-W, Park Y-H. Development of 3-D Nanofibrous Fibroin Scaffold with High Porosity by Electrospinning: Implications for Bone Regeneration. Biotechnol Lett. 2008; 30: 405–410. [PubMed: 17973083]

(12). Das S, Pati F, Choi Y-J, Rijal G, Shim J-H, Kim SW, Ray AR, Cho D-W, Ghosh S. Bioprintable, Cell-laden Silk Fibroin–Gelatin Hydrogel Supporting Multilineage Differentiation of Stem Cells for Fabrication of Three-Dimensional Tissue Constructs. Acta Biomater. 2015; 11: 233–246. [PubMed: 25242654]

(13). Zhang YS, Yue K, Aleman J, Moghaddam KM, Bakht SM, Yang J, Jia W, Dell'Erba V, Assawes P, Shin SR, Dokmeci MR, et al. 3D Bioprinting for Tissue and Organ Fabrication. Ann Biomed Eng. 2017; 45: 148–163. DOI: 10.1007/s10439-016-1612-8 [PubMed: 27126775]

(14). Farokhi M, Mottaghitalab F, Samani S, Shokrgozar MA, Kundu SC, Reis RL, Fatahi Y, Kaplan DL. Silk Fibroin/hydroxyapatite Composites for Bone Tissue Engineering. Biotechnol Adv. 2018; 36: 68–91. [PubMed: 28993220]

(15). Rockwood DN, Preda RC, Yücel T, Wang X, Lovett ML, Kaplan DL. Materials Fabrication from Bombyx mori Silk Fibroin. Nat Protoc. 2011; 6: 1612. doi: 10.1038/nprot.2011.379 [PubMed: 21959241]

(16). Maleki H, Montes S, Hayati-Roodbari N, Putz F, Huesing N. Compressible, Thermally Insulating, and Fire Retardant Aerogels through Self-Assembling Silk Fibroin Biopolymers Inside a Silica Structure—An Approach towards 3D Printing of Aerogels. ACS Appl Mater Interfaces. 2018; 10: 22718–22730. DOI: 10.1021/acsami.8b05856 [PubMed: 29864277]

(17). Hüsing N, Schubert U. Aerogels—Airy Materials: Chemistry, Structure, and Properties. Angew Chem Int Ed. 1998; 37: 22–45. [PubMed: 29710971]

(18). Yin, W, Rubenstein, DA. Aerogels Handbook. Aegerter, MA, Leventis, N, Koebel, MM, editors. Springer; 2011. 683–694.

(19). Szabó B, Kiss L, Manó S, Jónás Z, Lázár I, Fábián I, Dezso B, Csernátony Z. The Examination of Aerogel Composite Artificial Bone Substitutes in Animal Models. Biomech Hung. 2013. 52–63.

(20). Salerno A, Diéguez S, Diaz-Gomez L, Gómez-Amoza JL, Magariños B, Concheiro A, Domingo C, Alvarez-Lorenzo C, García-González CA. Synthetic Scaffolds with Full Pore Interconnectivity for Bone Regeneration Prepared by Supercritical Foaming Using Advanced Biofunctional Plasticizers. Biofabrication. 2017; 9 [PubMed: 28604361]

(21). Mallepally RR, Marin MA, Surampudi V, Subia B, Rao RR, Kundu SC, McHugh MA. Silk Fibroin Aerogels: Potential Scaffolds for Tissue Engineering Applications. Biomed Mater. 2015; 10 [PubMed: 25953953]

(22). Diaz-Gomez L, García-González CA, Wang J, Yang F, Aznar-Cervantes S, Cenis JL, Reyes R, Delgado A, Évora C, Concheiro A, Alvarez-Lorenzo C. Biodegradable PCL/Fibroin/Hydroxyapatite Porous Scaffolds Prepared by Supercritical Foaming for Bone Regeneration. Int J Pharm. 2017; 527: 115–125. [PubMed: 28539234]

(23). Martins M, Barros AA, Quraishi S, Gurikov P, Raman SP, Smirnova I, Duarte ARC, Reis RL. Preparation of Macroporous Alginate-based Aerogels for Biomedical Applications. J Supercrit Fluids. 2015; 106: 152–159.

(24). Zhou C, Yang K, Wang K, Pei X, Dong Z, Hong Y, Zhang X. Combination of Fused Deposition Modeling and Gas Foaming Technique to Fabricated Hierarchical Macro/Microporous Polymer Scaffolds. Mater Des. 2016; 109: 415–424.

(25). Maleki H, Durães L, Portugal A. An Overview on Silica Aerogels Synthesis and Different Mechanical Reinforcing Strategies. J Non-Cryst Solids. 2014; 385: 55–74.

(26). Maleki H, Durães L, Portugal A. Synthesis of Mechanically Reinforced Silica Aerogels via Surface-Initiated Reversible Addition-Fragmentation Chain Transfer (RAFT) Polymerization. J Mater Chem A. 2015; 3: 1594–1600.

(27). Zhao S, Malfait WJ, Demilecamps A, Zhang Y, Brunner S, Huber L, Tingaut P, Rigacci A, Budtova T, Koebel MM. Strong, Thermally Superinsulating Biopolymer–Silica Aerogel Hybrids by Cogelation of Silicic Acid with Pectin. Angew Chem Int Ed. 2015; 54: 14282–14286. [PubMed: 26447457]

(28). Maleki H, Whitmore L, Hüsing N. Novel Multifunctional Polymethylsilsesquioxane–Silk fibroin Aerogel Hybrids for Environmental and Thermal Insulation Applications. J Mater Chem A. 2018; 6: 12598–12612. DOI: 10.1039/c8ta02821d [PubMed: 30713688]

(29). Hayase G, Kanamori K, Abe K, Yano H, Maeno A, Kaji H, Nakanishi K. Polymethylsilsesquioxane–Cellulose Nanofiber Biocomposite Aerogels with High Thermal Insulation, Bendability, and Superhydrophobicity. ACS Appl Mater Interfaces. 2014; 6: 9466–9471. [PubMed: 24865571]

(30). Maleki H, Huesing N. Silica-Silk fibroin Hybrid (Bio)aerogels: Two-step Versus One-step Hybridization. J Sol gel Sci Technol. 2019; doi: 10.1007/s10971-019-04933-4 [PubMed: 34720431]

(31). Wubneh A, Tsekoura EK, Ayranci C, Uludağ H. Current State of Fabrication Technologies and Materials for Bone Tissue Engineering. Acta Biomater. 2018; 80: 1–30. [PubMed: 30248515]

(32). Porrelli D, Travan A, Turco G, Marsich E, Borgogna M, Paoletti S, Donati I. Alginate–Hydroxyapatite Bone Scaffolds with Isotropic or Anisotropic Pore Structure: Material Properties and Biological Behavior. Macromol Mater Eng. 2015; 300: 989–1000.

(33). Wang D, Romer F, Connell L, Walter C, Saiz E, Yue S, Lee PD, McPhail DS, Hanna JV, Jones JR. Highly Flexible Silica/chitosan Hybrid Scaffolds with Oriented Pores for Tissue Regeneration. J Mater Chem B. 2015; 3: 7560–7576. [PubMed: 32262640]

(34). Mitchell GR, Tojeira A. Role of Anisotropy in Tissue Engineering. Procedia Eng. 2013; 59: 117–125.

(35). Davidenko N, Gibb T, Schuster C, Best SM, Campbell JJ, Watson CJ, Cameron RE. Biomimetic Collagen Scaffolds with Anisotropic Pore Architecture. Acta Biomater. 2012; 8: 667–676. [PubMed: 22005330]

(36). Mathieu LM, Mueller TL, Bourban P-E, Pioletti DP, Müller R, Månson J-AE. Architecture and Properties of Anisotropic Polymer Composite Scaffolds for Bone Tissue Engineering. Biomaterials. 2006; 27: 905–916. [PubMed: 16051346]

(37). Pircher N, Fischhuber D, Carbajal L, Strauss C, Nedelec J-M, Kasper C, Rosenau T, Liebner F. Preparation and Reinforcement of Dual-Porous Biocompatible Cellulose Scaffolds for Tissue Engineering. Macromol Mater Eng. 2015; 300: 911–924. [PubMed: 26941565]

(38). Mieszawska AJ, Fourligas N, Georgakoudi I, Ouhib NM, Belton DJ, Perry CC, Kaplan DL. Osteoinductive Silk–Silica Composite Biomaterials for Bone Regeneration. Biomaterials. 2010; 31: 8902–8910. DOI: 10.1016/j.biomaterials.2010.07.109 [PubMed: 20817293]

(39). Gaharwar AK, Mihaila SM, Swami A, Patel A, Sant S, Reis RL, Marques AP, Gomes ME, Khademhosseini A. Bioactive Silicate Nanoplatelets for Osteogenic Differentiation of Human Mesenchymal Stem Cells. Advanced Mater. 2013; 25: 3329–3336. [PubMed: 23670944]

(40). Nishihara H, Mukai SR, Yamashita D, Tamon H. Ordered Macroporous Silica by Ice Templating. Chem Mater. 2005; 17: 683–689.

(41). Loh QL, Choong C. Three-Dimensional Scaffolds for Tissue engineering Applications: Role of Porosity and Pore Size. Tissue Eng Part B, Reviews. 2013; 19: 485–502. DOI: 10.1089/ten.teb.2012.0437 [PubMed: 23672709]

(42). Zhang Q, Yang X, Li P, Huang G, Feng S, Shen C, Han B, Zhang X, Jin F, Xu F, Lu TJ. Bioinspired Engineering of Honeycomb Structure – Using Nature to Inspire Human Innovation. Prog Mater Sci. 2015; 74: 332–400.

(43). Maleki H, Durães L, Portugal A. Synthesis of Lightweight Polymer-reinforced Silica Aerogels with Improved Mechanical and Thermal Insulation Properties for Space Applications. Microporous Mesoporous Mater. 2014; 197: 116–129.

(44). Naskar D, Ghosh AK, Mandal M, Das P, Nandi SK, Kundu SC. Dual Growth Factor Loaded Nonmulberry Silk fibroin/Carbon Nanofiber Composite 3D Scaffolds for In vitro and In vivo Bone Regeneration. Biomaterials. 2017; 136: 67–85. [PubMed: 28521202]

(45). Lyu S, Untereker D. Degradability of Polymers for Implantable Biomedical Devices. Int J Mol Sci. 2009; 10: 4033–4065. DOI: 10.3390/ijms10094033 [PubMed: 19865531]

(46). Tseng P, Napier B, Zhao S, Mitropoulos AN, Applegate MB, Marelli B, Kaplan DL, Omenetto FG. Directed Assembly of Bio-inspired Hierarchical Materials with Controlled Nanofibrillar Architectures. Nat Nanotechnol. 2017; 12: 474. [PubMed: 28250472]

(47). Zhang K, Fan Y, Dunne N, Li X. Effect of Microporosity on Scaffolds for Bone Tissue Engineering. Regen Biomater. 2018; 5: 115–124. DOI: 10.1093/rb/rby001 [PubMed: 29644093]

(48). Shahbazi M-A, Almeida PV, Correia A, Herranz-Blanco B, Shrestha N, Mäkilä E, Salonen J, Hirvonen J, Santos HA. Intracellular Responsive Dual Delivery by Endosomolytic Polyplexes Carrying DNA Anchored Porous Silicon Nanoparticles. J Control Release. 2017; 249: 111–122. [PubMed: 28159519]

(49). Brockman KS, Kizhakkedathu JN, Santerre JP. Hemocompatibility Studies on a Degradable Polar Hydrophobic Ionic Polyurethane (D-PHI). Acta Biomaterialia. 2017; 48: 368–377. [PubMed: 27818307]

(50). DEB, S. Cellular Response to Biomaterials. Silvio, LD, editor. Vol. Chapter 2. Woodhead Publishing Series in Biomaterials; 2009. 28–60.

(51). Naskara D, Ghosha AK, Mandalb M, Dasc P, Nandic SK, Kundu SC. Dual Growth Factor Loaded Nonmulberry Silk fibroin/Carbon Nanofiber Composite 3D Scaffolds for In vitro and In vivo Bone Regeneration. Biomaterials. 2017; 136: 67–85. [PubMed: 28521202]

(52). Langer R. Tissue Engineering: Status and Challenges. Biomed J Regen Med. 2000; 1: 5–6.

(53). Sabri F, Sebelik ME, Meacham R, Boughter JD Jr, Challis MJ, Leventis N. In Vivo Ultrasonic Detection of Polyurea Crosslinked Silica Aerogel Implants. PLOS ONE. 2013; 8 (6) e66348. doi: 10.1371/journal.pone.0066348 [PubMed: 23799093]

(54). Allison SW, Baker ES, Lynch KJ, Sabri F. In Vivo X-Ray Imaging of Phosphor-Doped PDMS and Phosphor-Doped Aerogel Biomaterials. Int J Polym Mater Poly Mater. 2015; 64: 823–830. DOI: 10.1080/00914037.2015.1030652

(55). Sabri F, Boughter JD Jr, Gerth D, Skalli O, Phung T-CN, Tamula G-RM, Leventis N. Histological Evaluation of the Biocompatibility of Polyurea Crosslinked Silica Aerogel Implants in a Rat Model: A Pilot Study. PLOS ONE. 2012; 7: e50686. doi: 10.1371/journal.pone.0050686 [PubMed: 23251378]

(56). Sabri F, Gerth D, Tamula G-RM, Phung T-CN, Lynch KJ, Boughter JD Jr. Novel Technique for Repair of Severed Peripheral Nerves in Rats Using Polyurea Crosslinked Silica Aerogel Scaffold. J Invest Surg. 2014; 27: 294–303. [PubMed: 24833437]

Europe PMC Funders Author Manuscripts

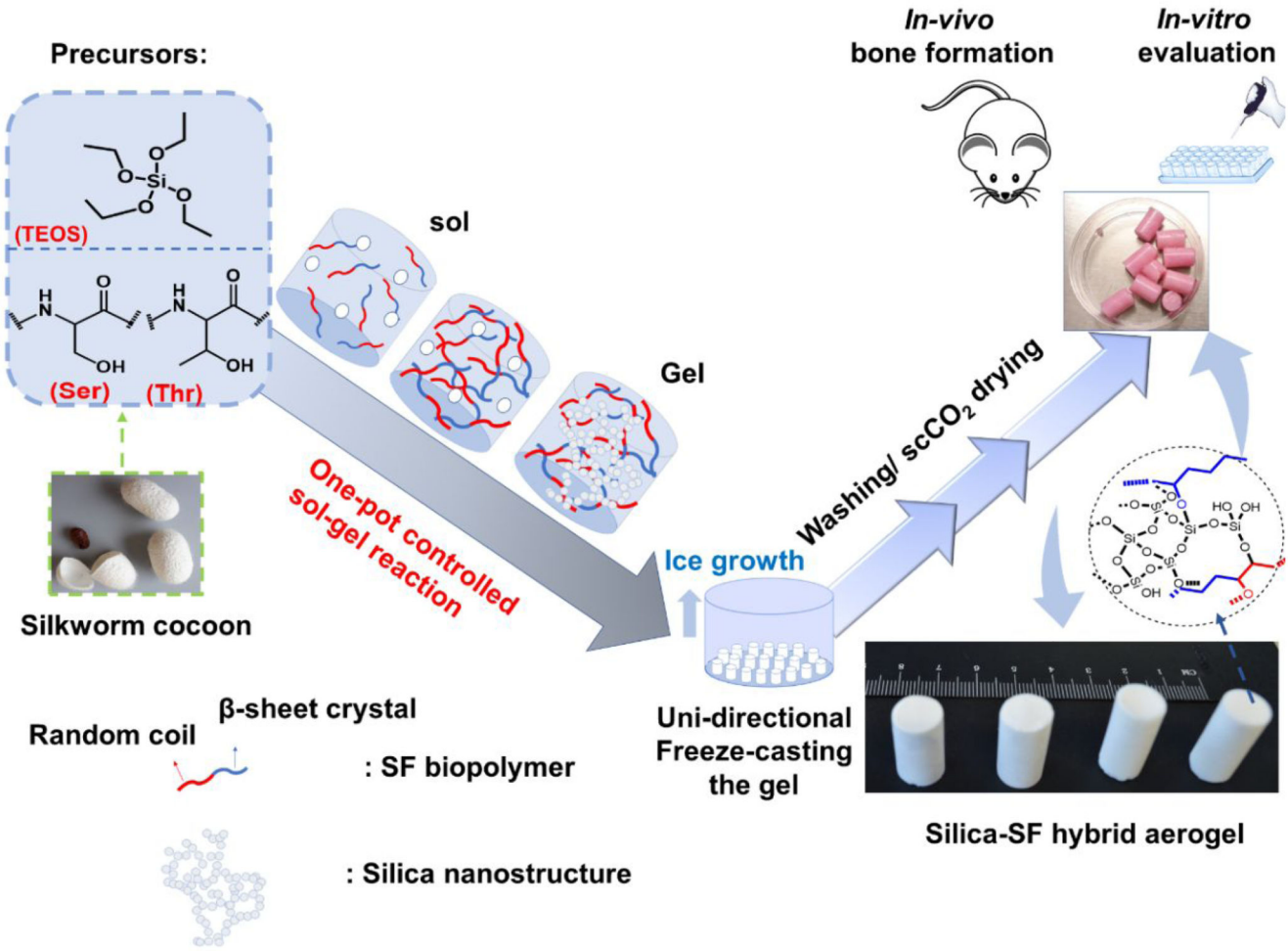

Figure 1.

Schematic illustration of synthesis procedure for silica-SF aerogel hybrid scaffold through sol-gel reaction, unidirectional freeze-casting and supercritical drying approach

Europe PMC Funders Author Manuscripts

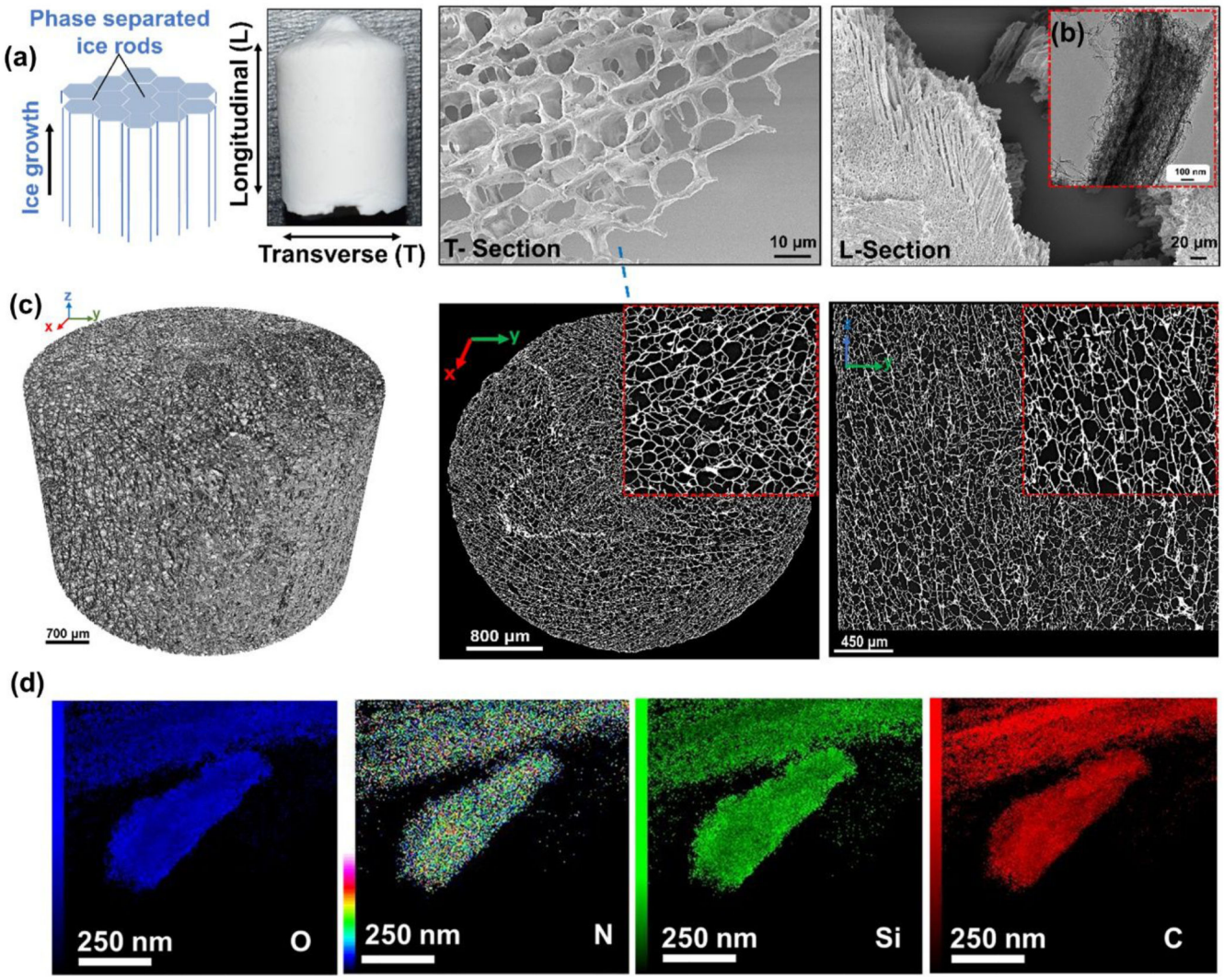

Figure 2.

Microstructural and compositional characteristic of Silica-SF aerogel hybrid scaffold with a) SEM, b) TEM, c) μ-CT scans and 3D reconstruction, and d) TEM-EDX elemental mapping.

Europe PMC Funders Author Manuscripts

Europe PMC Funders Author Manuscripts

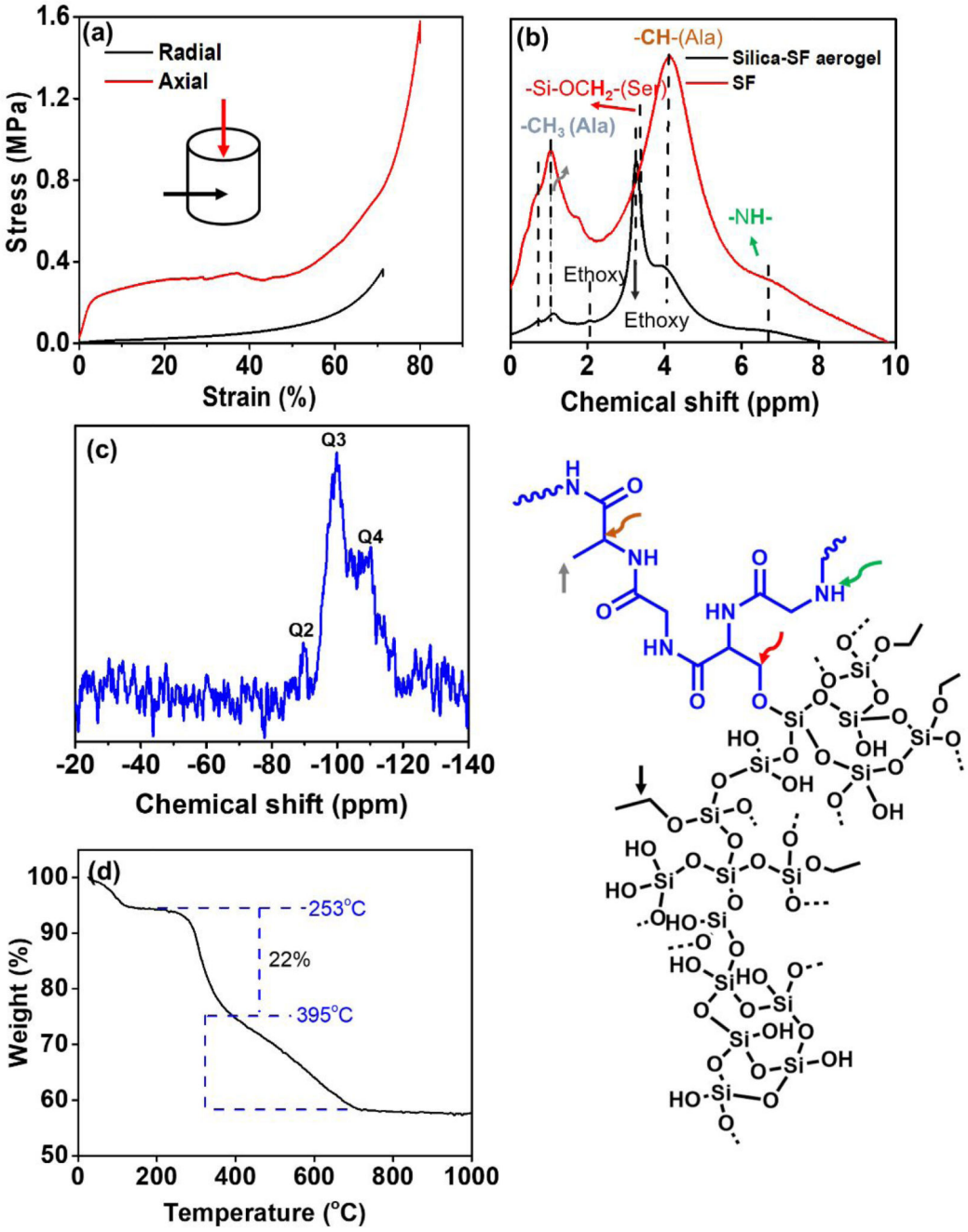

Figure 3.

(a) Stress-strain curve, solid-state MAS (b) ^{1}H and (c) ^{29}Si NMR spectroscopies (including the proposed molecular structure of silica-SF aerogel), and (d) thermogravimetric (TG) analysis of silica-SF aerogel scaffold. SF aerogel in (b) has undergone to the same freezing conditions as silica-SF aerogel.

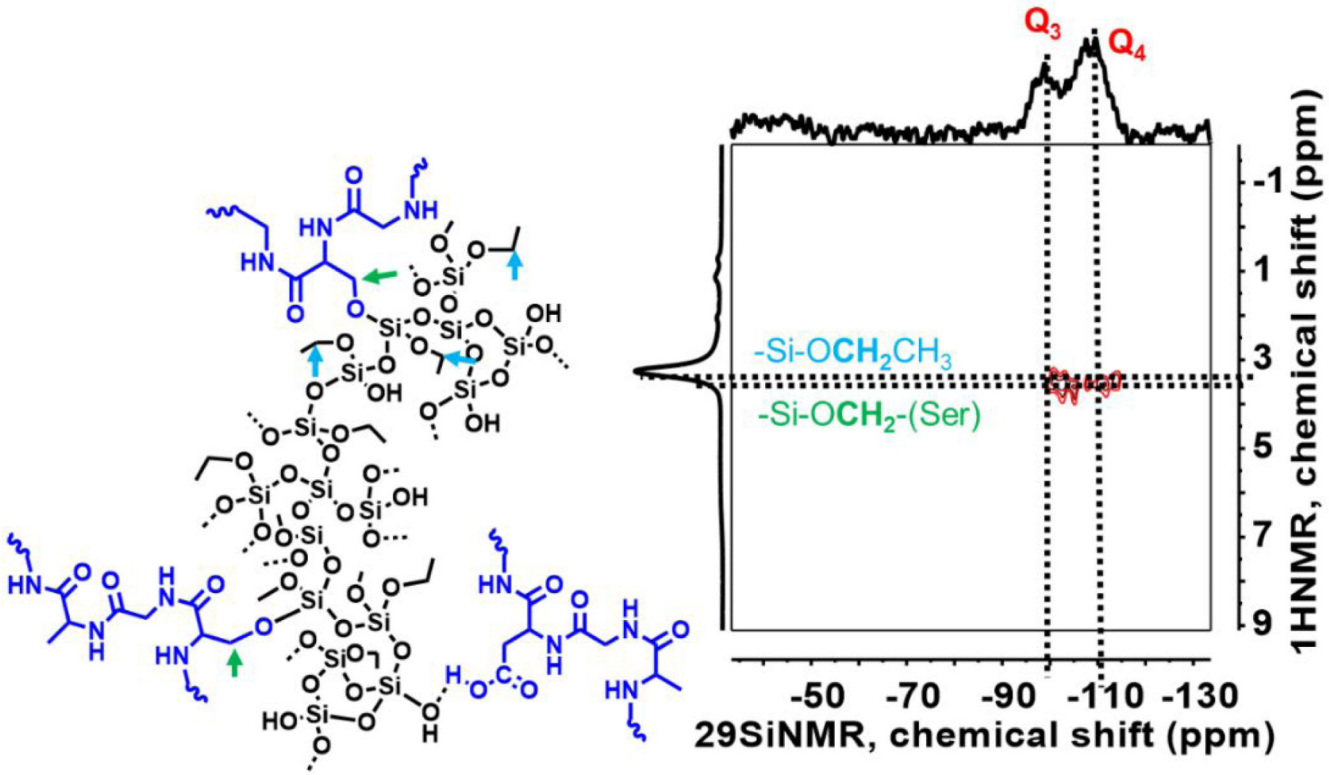

Figure 4.
^{1}H-^{29}Si heteronuclear correlation MAS NMR spectroscopy of silica-SF aerogel.

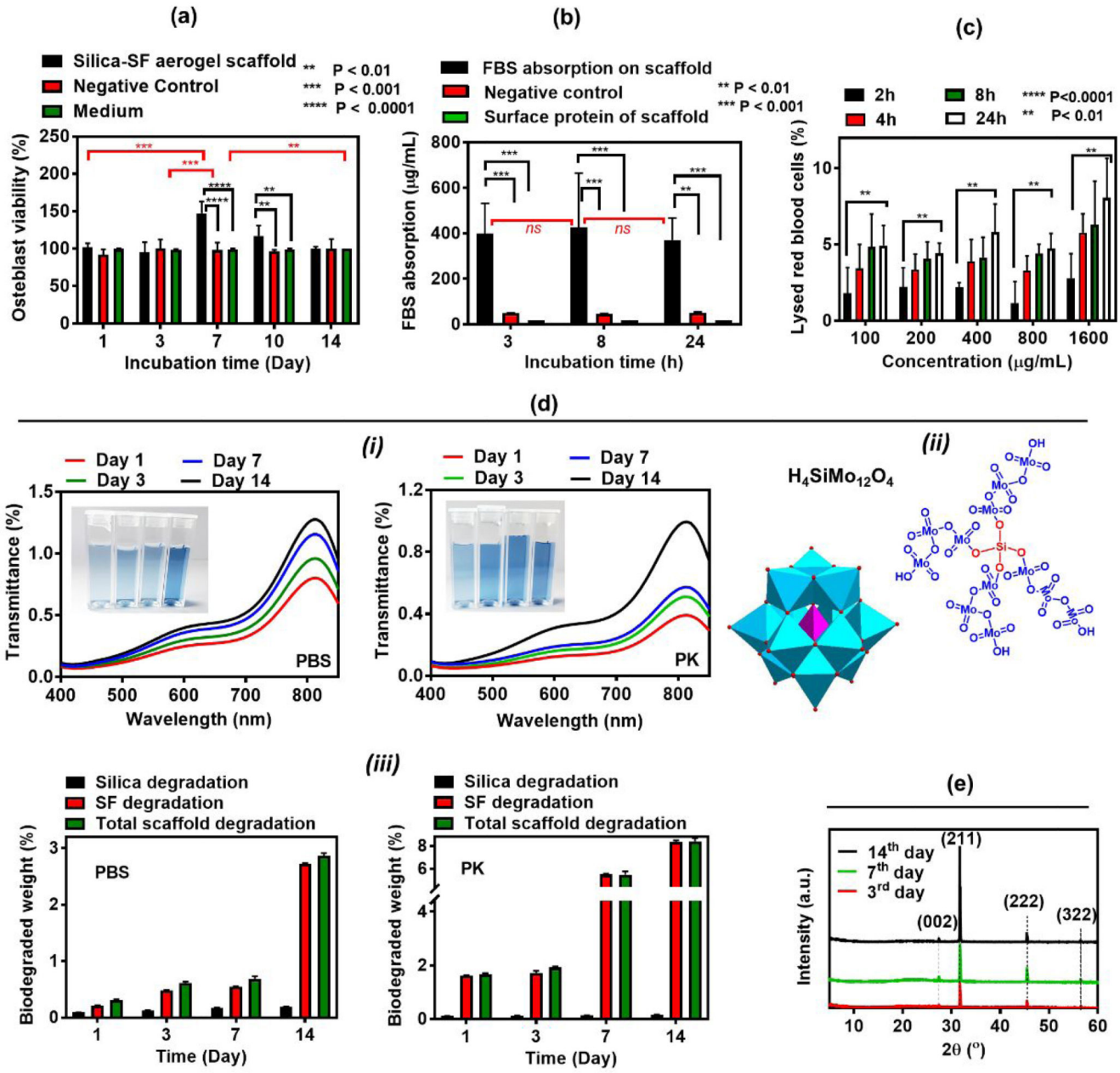

Figure 5.

(a) Cell toxicity, (b) protein adsorption, (c) hemolysis (d) degradation studies for silica and SF component (*i*) including the structure of silicomolybdic acid complex (*ii*) and its UV–visible spectra in different degradation solvents, PBS and PK, (e) XRD diffractogram for biomineralization of silica-SF aerogel scaffold

Europe PMC Funders Author Manuscripts

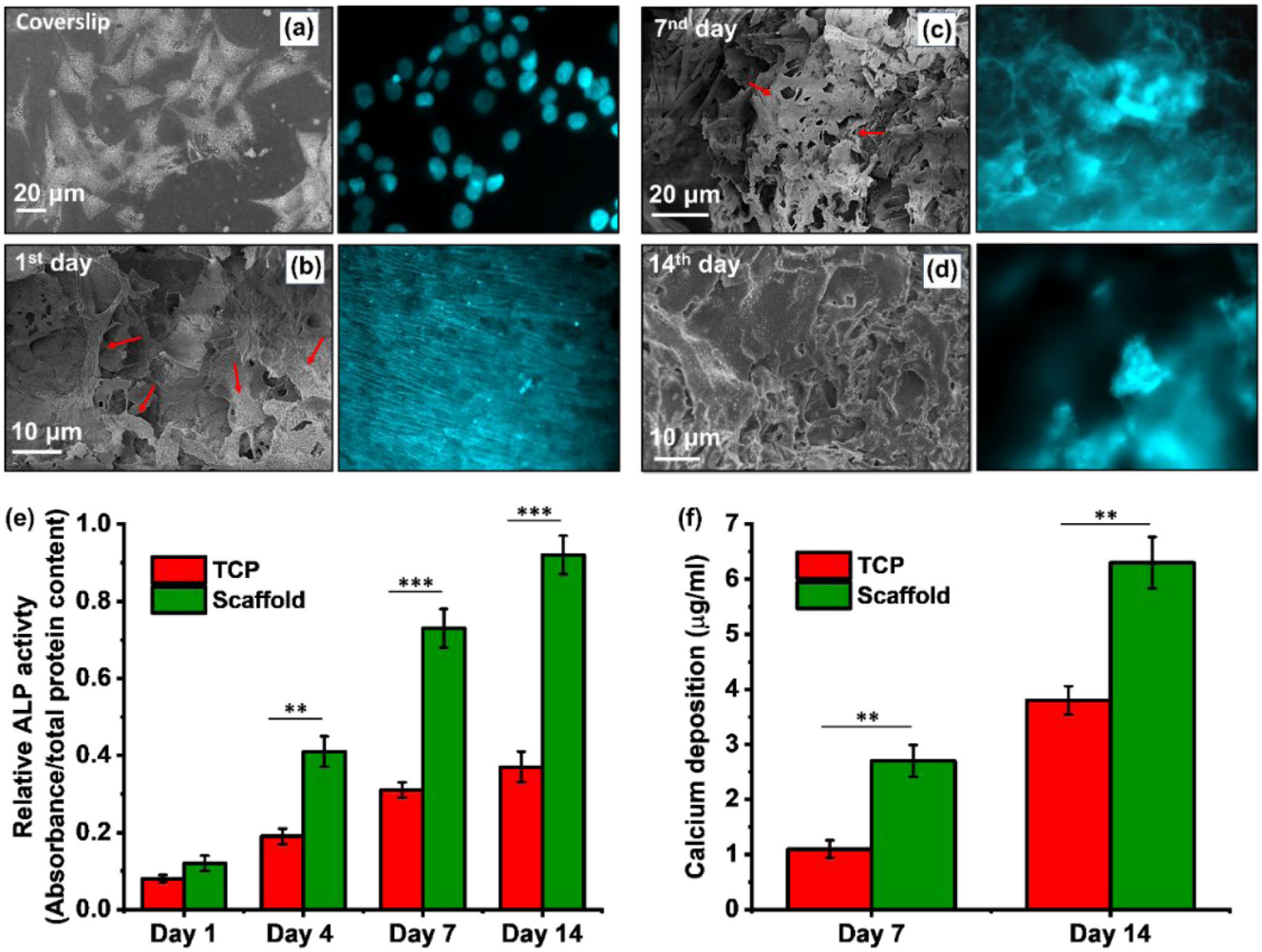

Figure 6.

(a-d) SEM and fluorescence microscopy images (Hoechst 33342 staining) of cell growth and attachment on scaffold over 14 days. (e) ALP activity and (f) calcium content of MG-63 cultured on the scaffold for 14 days. Statistical comparisons were performed with respect to TCP, which represent the cells grown in the 2D culture flask.

Europe PMC Funders Author Manuscripts

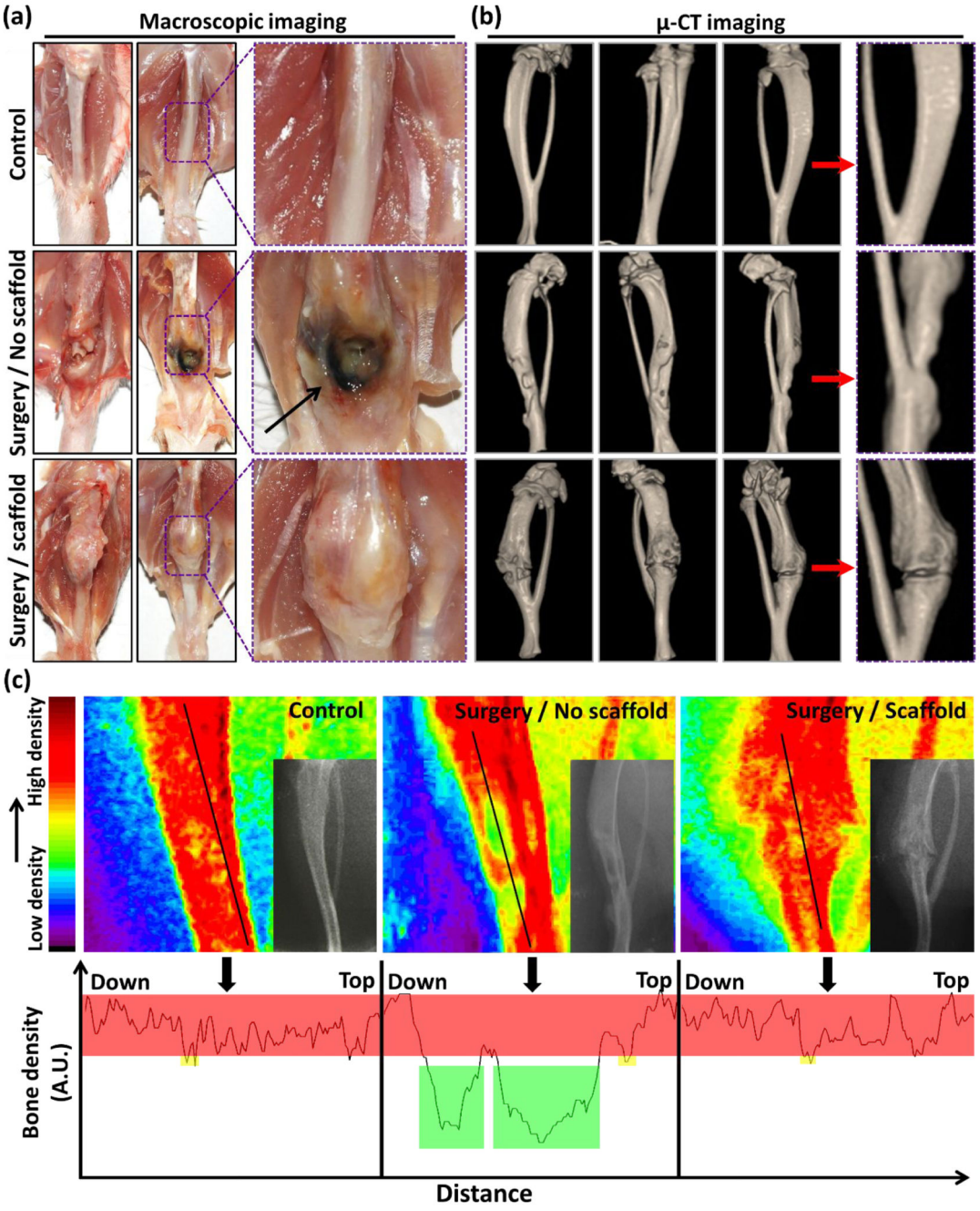

Figure 7.

(a) Macroscopic view of the scaffold implanted site after 25 days of placement in the region of the rat femur. (b) Micro-CT images of the bone in the control group without creating any defect as well as defect sites without and with scaffold after 25 days of surgery and implantation. The yellow coloured area shows the areas without bone formation in the animals with bone defect but no scaffold implantation. (c) Counterplot colour-based analysis of the bone density based on the radiographic images of the different tested groups shown in the bottom-right area of each counterplot image. The red area represents high density of

the bone while green colour demonstrates the parts without any bone formation. The bone density profile of the bone areas covered by the black line drawn in counterplot colour-based bone density analysis.

Europe PMC Funders Author Manuscripts

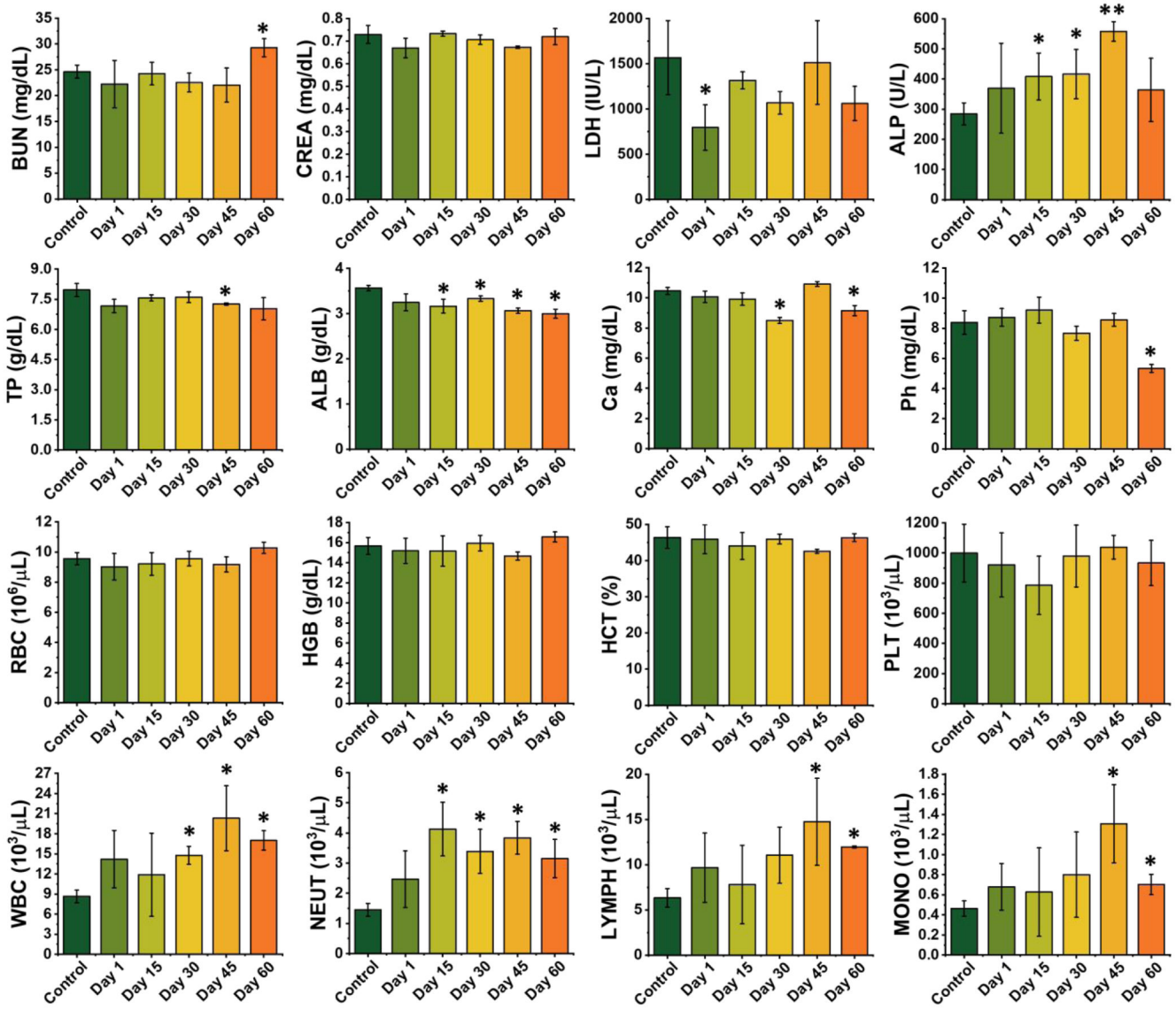

Figure 8.

In vivo toxicity evaluation. Hematological index and biochemical blood analysis of the rat at 1, 15, 30, 45, and 60 days post scaffold implantation is compared to the control group that was not subjected to surgery. The results show the mean and SD of BUN, CREA, LDH, ALP, TP, ALB, Ca, Ph, RBC, HGB, HCT, PLT, WBC, neutrophils (NEUT), lymphocytes (LYMPH) and monocytes (MONO) at different time points post scaffold implantation.

Table 1

Freezing conditions along with key physical, structural and mechanical properties of aerogel scaffold

Aerogel	ν_f [cm h^{-1}]	T_f [°C]	ρ_b *a* [g cm^{-3}]	ε [%] *b*	S_{BET} *c* [m^2 g^{-1}]	Max.Strength, δ [MPa]	Young' s Module,ε [MPa]	Pore diameter, $D_{p,BJH}$ [nm]	Macro-pore *d*, φ (μm)
silica-SF-10-33	33	-10	0.115	91	493	0.39	4.03	18	1.10±0.31
silica-SF-10-66	66	-10	0.108	93	531	0.36	4.24	16	0.52±0.14
silica-SF-196-33	33	-196	0.075	94	433	1.6	7.3	17	17.84±2.75
silica-SF-196-66	66	-196	0.077	94	466	0.92	6.7	16	6.35±2.63

a Bulk density (ρ_{bulk})

b porosity (ε %)

c specific surface area (S_{BET})

d macro-sized pore diameter (obtained from SEM micrographs).